Geophysical Research Letters

RESEARCH LETTER
10.1029/2019GL084710

Laboratory Experiments on Internal Solitary Waves in Ice-Covered Waters

Magda Carr[1], Peter Sutherland[2], Andrea Haase[3], Karl-Ulrich Evers[4], Ilker Fer[5], Atle Jensen[6], Henrik Kalisch[7], Jarle Berntsen[7], Emilian Părău[8],Øyvind Thiem[9], and Peter A. Davies[10]

[1]School of Mathematics, Statistics & Physics, Newcastle University, Newcastle upon Tyne, UK, [2]IFREMER, CNRS, IRD, Laboratoire d'Océanographie Physique et Spatiale (LOPS), IUEM, Université de Bretagne Occidentale, Brest, France, [3]HSVA, Hamburgische Schiffbau-Versuchsanstalt GmbH, Hamburg, Germany, [4]solutions4arctic, Hamburg, Germany, [5]Geophysical Institute, University of Bergen, Bergen, Norway, Department of Mathematics,[6]University of Oslo, Oslo, Norway, [7]Department of Mathematics, University of Bergen, Bergen, Norway, [8]School of Mathematics, University of East Anglia, Norwich, UK, [9]Norwegian Public Roads Administration, Bergen, Norway, [10]Department of Civil Engineering, University of Dundee, Dundee, UK

Abstract Internal solitary waves (ISWs) propagating in a stably stratified two-layer fluid in which the upper boundary condition changes from open water to ice are studied for grease, level, and nilas ice. The ISW-induced current at the surface is capable of transporting the ice in the horizontal direction. In the level ice case, the transport speed of, relatively long ice floes, nondimensionalized by the wave speed is linearly dependent on the length of the ice floe nondimensionalized by the wave length. Measures of turbulent kinetic energy dissipation under the ice are comparable to those at the wave density interface. Moreover, in cases where the ice floe protrudes into the pycnocline, interaction with the ice edge can cause the ISW to break or even be destroyed by the process. The results suggest that interaction between ISWs and sea ice may be an important mechanism for dissipation of ISW energy in the Arctic Ocean.

Key Points:
- Internal solitary waves in partially ice-covered water are generated in the laboratory
- Internal solitary wave-induced currents can transport the ice horizontally
- In the laboratory, dissipation of turbulent kinetic energy under the ice is comparable to that at the wave density interface

Supporting Information:
- Supporting Information S1

Correspondence to:
M. Carr,
magda.carr@newcastle.ac.uk

Citation:
Carr, M., Sutherland, P., Haase, A., Evers, K.-U., Fer, I., Jensen, A., et al. (2019). Laboratory experiments on internal solitary waves in ice-covered waters. *Geophysical Research Letters*, *46*, 12,230–12,238. https://doi.org/10.1029/2019GL084710

Received 26 JUL 2019
Accepted 25 SEP 2019
Accepted article online 15 OCT 2019
Published online 13 NOV 2019

1. Introduction

Internal waves (IWs) are ubiquitous in stratified water. They propagate through the stratified water column and, in the case of a two-layer fluid, along the density interface. In the Arctic Ocean, IW dynamics (i) constitute an integral part of the circulation and thermodynamics (Levine et al., 1985; Sandven & Johannessen, 1987) and (ii) play an important role in the vertical mixing of the upper layers (D'Asaro & Morison, 1992; Fer, 2014; Kirillov, 2006), which, in turn, affects renewal of nutrients and sea ice evolution.

The majority of past observations have been of low-frequency IWs, based on sparse in situ measurements due to year-round sea ice cover. Recently, however, as a consequence of prolonged ice retreat, synthetic aperture radar observations have facilitated the mapping of high-frequency internal solitary waves (ISWs) in open water areas of the Arctic Ocean and its marginal seas (Kozlov et al., 2015, 2017; Zimin et al., 2016). The waves are typically nonlinear, rank-ordered packets in which the leading wave has an amplitude that is comparable to the upper layer depth.

A dominant generator of IWs is tidal flow over topography, where the energy of the surface tide is converted to the internal (baroclinic) tide, typically at semidiurnal frequencies. For most of the major tidal constituents, the Arctic is above the critical latitude where the propagation of linear IWs is suppressed by the Earth's rotation. Yet IWs have been observed in the Arctic Ocean, associated with increased turbulence (Padman & Dillon, 1991; Rippeth et al., 2017). The mechanisms of generation and energy pathways to turbulence are not yet fully understood. The frequency of the IW packets and their characteristic spatial scales suggest that the majority are linked to the barotropic tide and are a consequence of a lee wave generation process first proposed by Vlasenko et al. (2003). Recent idealized modeling and field observations (Rippeth et al., 2017) have supported the lee wave generation process and have linked such nonlinear IWs to enhanced mixing through collocated velocity microstructure measurements.

Enhanced levels of dissipation of turbulent kinetic energy (TKE) are well documented over areas of sloping topography in the Arctic Ocean (D'Asaro & Morison, 1992; Fer et al., 2010; Padman & Dillon, 1991;

Rainville & Winsor, 2008; Rippeth et al., 2015). This is in contrast to the central Arctic Ocean, which is remarkably quiescent (Fer, 2009; Lincoln et al., 2016) and has shown a lack of significant long-term trends despite changes in sea ice concentration (Guthrie et al., 2013). By synthesizing a pan-Arctic data set, Rippeth et al. (2015) suggest tidal conversion as the main source of enhanced dissipation rates and vertical heat fluxes, despite much of the Arctic Ocean lying poleward of the critical latitude. Short scale IWs (which are not affected by the Earth's rotation) have been proposed as the agency responsible for the transfer of energy from the tide to turbulent mixing at such latitudes (Rippeth et al., 2017).

IWs are known to cause flexure of sea ice (Czipott et al., 1991; Marchenko et al., 2010), and theoretical studies (Muench et al., 1983; Saiki & Mitsudera, 2016) suggest they are responsible for the formation of ice bands in the marginal ice zone. The annual variation of the Arctic ice edge is monitored carefully (i) to assess climate change and (ii) for a variety of practical reasons involving sea traffic, fisheries, offshore operations, and military marine activities. There is a clear interplay between IWs and sea ice, and motivation to study the topic is wide ranging, yet very few dedicated investigations exist.

While field observations provide insight into IW dynamics in the Arctic Ocean, none to date isolate the effects of individual ice, ocean and wind parameters. Moreover, field measurements in the marginal ice zone are particularly challenging and hazardous due to variable ice thickness and high potential for ice floe breakup. In addition, the harshness of the environment and the remoteness of the location can limit observations, especially in periods of ice cover. Synthetic aperture radar imagery has provided valuable new insight, but its use is restricted to areas of open water and to climatic conditions being favorable for the observations to be made. There is a clear need, therefore, to supplement field work with modeling studies. In this study, a laboratory investigation of ISWs in a two-layer stratified flow propagating from open water to under ice is presented. The ice type is varied, and the interaction between the ISW and ice was investigated. The aim of the paper is to model physically the interaction of an ISW with different types of ice and hence demonstrate that this interaction can lead to dissipation of ISW energy through different pathways including (i) boundary friction at the underside of the ice, (ii) transportation of the ice, and (iii) deformation of the wave form. The study is primarily illustrative and qualitative, a full sweep of parameter space being beyond the scope of the current paper. This is the first time that ISWs have been generated under ice in a laboratory setting.

2. Experimental Setup and Procedure

2.1. Physical Arrangement and Wave Generation

The experiments took place in a wave flume 6 m in length, 0.47 m in width, and 0.6 m in depth. The flume was built within the HSVA Arctic Environmental Test Basin facility in Hamburg. The flume was of plexiglass construction to allow visualization from the side and illumination from below. It was filled with homogeneous salt water of prescribed density $\rho_3 = 1,045$ kg/m^3. Less dense brine solution of density $\rho_1 = 1,025$ kg/m^3 was then slowly added via an array of floating surface sponges. Consequently, an interface (pycnocline) between the two fluids formed in which the density varied as a linear function of depth z. The density range was chosen such that neutrally buoyant particles could be suspended throughout the depth of the water column enabling flow visualization and measurement (see section 2.4). A gate G was inserted at the upstream end of the tank (see Figure 1) and lowered to approximately 1 cm above the bed of the flume. A fixed volume, V, of water of density ρ_1 was then added behind the gate. Due to hydrostatic balance, fluid of density ρ_3 flowed under the gate into the main section of the flume. Once the volume, V, had been added, the total fluid depth H, in the main section of the flume, was measured using a pre-set tape on the plexiglass window. The laboratory air temperature was kept just above 0°C while the flume was filled.

2.2. Ice Formation

After the flume had been stratified, different ice cover types were applied. A vast array of ice types can be found in the Arctic Ocean; hence the ice types investigated were chosen to cover as broad a range as practically possible. The laboratory was cooled to approximately −2°C or −15°C in cases where ice was added or made, respectively. The temperature and thickness of the ice were monitored throughout the duration of a given experiment. No change of form or melting was observed.

(i) **Model level ice** was formed from a 0.7% sodium chloride solution following the procedure outline in Evers (2015). During the freezing process, tiny air bubbles of diameter 200–500 μm were embedded into growing ice crystals. Due to the embedded air, the mechanical properties of the model ice (strength, elasticity,

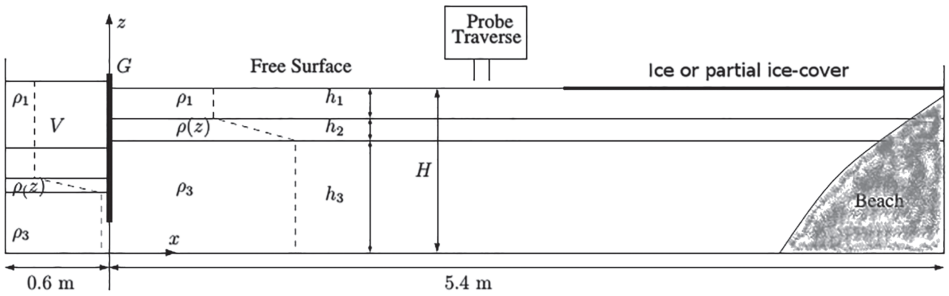

Figure 1. Schematic diagram (not to scale) of the laboratory arrangement.

fracture behavior, and density) were made as close as possible to the mechanical properties of ice prevailing in nature. In particular, the model ice had a density range of 782–803 kg/m^3 which is within the natural range for sea ice of 720–940 kg/m^3. Sections of level ice were cut and removed from the laboratory and kept in a cold storage unit. When required, the floes of level ice were carefully lowered into the stratified flume. The level ice floes had a length, $l_f \approx 1$ m, and two different thicknesses were considered, namely, $d_f = 0.013$ m and $d_f = 0.058$ m.

(ii) **Grease ice** was made by crushing stored model level ice and adding it carefully to the surface of the stratified water while taking care to disturb neither the pycnocline nor the upper layer. Individual pieces of grease ice had complex geometries and the typical length scale of a piece ranged from 0.001 to 0.05 m. These pieces were arranged such that a surface length of 2.65 m was covered by the ice and the total thickeness of the grease ice layer was approximately 0.02 m.

(iii) **Nilas ice** was made by reducing the air temperature in the laboratory (to −15°C) so that the surface of the water column froze. Open water sections were maintained by placing styrofoam at the surface during the freezing process. The styrofoam lids were removed just prior to an experiment commencing. The thickness of the nilas ice layer was approximately 0.006 m, and it covered a surface length of 2.69 m.

2.3. Wave Generation

ISWs were generated by the swift, smooth removal of the gate in the vertical direction. After a sorting distance of approximately 1 m, an ISW of depression propagated horizontally along the pycnocline into the main section of the tank. A beach (of polyether filter foam) was located at the downstream end of the flume to absorb some of the ISW energy, but a reflected ISW signal was still seen in all but one of the experimental runs. Once an experiment was finished and the water column stationary, the gate was re-inserted and a fixed volume of fluid of density ρ_1 was again added behind the gate so that a second run could be performed.

2.4. Flow Measurement and Flow Visualization

With the ice in place and the water column stationary, high precision microconductivity sensors (Munro & Davies, 2009) were used to measure the form of the stratification. The sensors were mounted on a rigid rack and pinion traverse system fitted with a potentiometer. The sensors were moved vertically through the water column, and density profiles were obtained by calibrating the potentiometer output and conductivity data against known values of height and fluid density, respectively.

Analysis was restricted to two dimensions, (x, z), where x denotes the horizontal direction and z the vertical direction, with the origin $x = 0$ corresponding to the horizontal location of the gate and $z = 0$ to the bed of the flume (see Figure 1). The vertical extent of the upper, middle, and lower layers of the stratification were denoted by h_1, h_2, and h_3, respectively. The ratio of the layer thicknesses, and in particular the upper two-layer thicknesses, was chosen to be similar to those observed in the Eurasian Arctic shelf seas and slopes (Fer et al., 2010; Kozlov et al., 2014; Padman & Dillon, 1991). The formation of the stratification was difficult to control precisely due to (i) disturbances during filling, (ii) disturbances when adding the ice, and (iii) differences in filling times. As a result, the layer depths varied such that $h_3 = 0.32 \pm 0.01$ m, $h_2 = 0.04 \pm 0.01$ m, and $h_1 = 0.045 \pm 0.002$ m for the first run of a given experiment, and $h_3 = 0.32 \pm 0.01$ m, $h_2 = 0.04 \pm 0.01$ m, and $h_1 = 0.055 \pm 0.002$ m for the second run.

A light source (intense LED strip passed through a double slit) was placed beneath the transparent base of the tank. It generated a thin, vertical column of light which was arranged to illuminate a two-dimensional slice of the flow field in the midplane of the flume aligned with the x axis. The water column was seeded

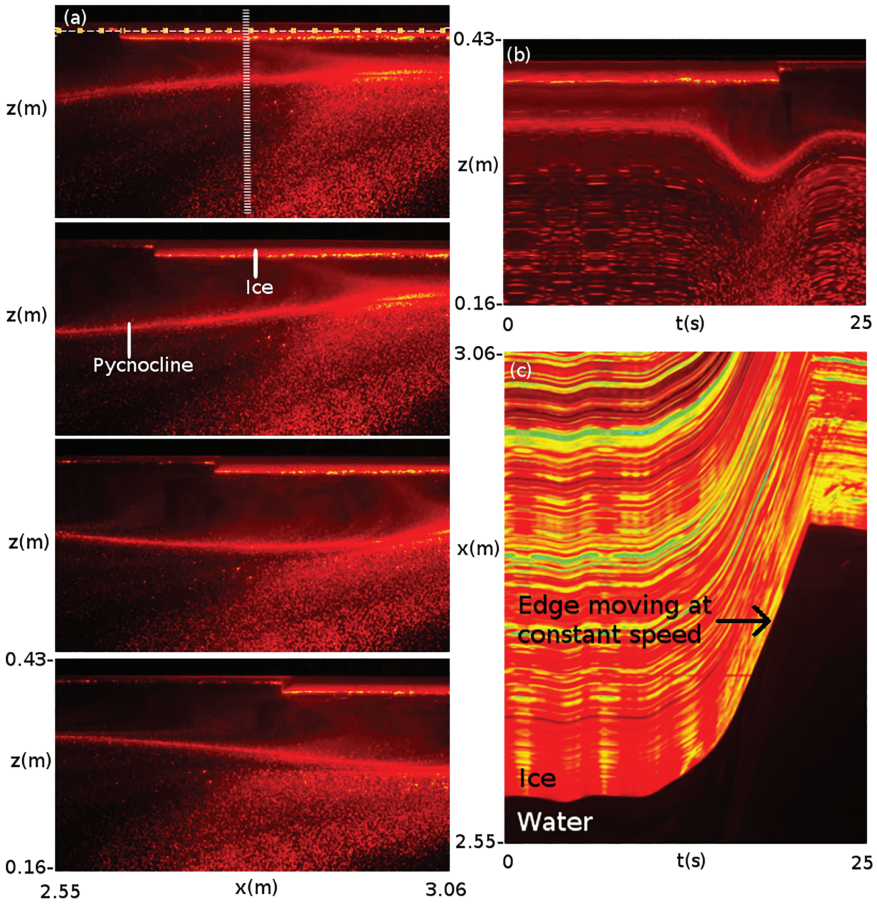

Figure 2. (a) Series of still experimental images with level ice of dimensions d_f = 0.013 m and l_f = 0.95 m, showing light intensity, ordered sequentially in time from top to bottom at intervals of Δt=2.2 s, (b) vertical time series made from column marked by vertical dashed line in (a), and (c) horizontal time series made from row marked by horizontal dot-dashed line in (a) rotated through 90° anticlockwise.

with neutrally buoyant, light-reflecting tracer particles of "Pliolite" having diameters in the range 150–300 μm (Fructus et al., 2009). Motions within the vertical light sheet were viewed and recorded from the side using three fixed digital video cameras set up outside the flume. The cameras (UNIQ UP-1830-CL-12B) had a spatial resolution of 1372 × 1372 pixels and a capture rate of 30 frames per second. The three cameras were synchronized in time, and two were positioned to have overlapping fields of view.

The software package *DigiFlow* (Dalziel et al., 2007) was used to process the digital video records. The time series function of *DigiFlow* was used to measure wave phase speed c, wave amplitude a, wave length λ, and wave-induced ice floe speed c_f. The particle image velocimetry (PIV) function of *DigiFlow* was used to calculate continuous synoptic velocity and vorticity field data along the illuminated cross-section in the middle of the flume. The average ice thickness d_f and ice length l_f were measured with calipers and a rule, respectively. The width of the ice was as close as practically possible to the width of the tank.

3. Results

3.1. Ice Motion

Provided the ice was free to move, the ISW-induced current at the surface transported the ice horizontally in the same direction as that of wave propagation. This is illustrated in Figure 2a in which still images from an experiment with level ice of dimensions d_f = 0.013 m and l_f = 0.95m are presented. The images show light scattered from the neutrally buoyant tracer particles and are displayed in a false color scheme to optimize the visualization. The ice at the surface can be seen by light reflected off its underside and the pycnocline can be identified by the clustering of tracer particles at the density interface. The ISW was propagated from left to right.

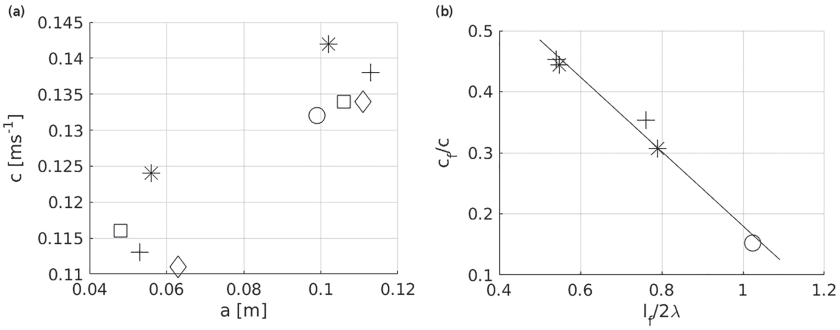

Figure 3. (a) Wave phase speed c versus wave amplitude a and (b) nondimensional wave-induced level ice floe speed c_f/c versus nondimensional level ice floe length $l_f/2\lambda$. Different symbols correspond to different ice types and dimensions as follows: $*$ level ice with $d_f = 0.013$ m and $l_f = 0.95$ m; $+$ level ice with $d_f = 0.058$ m and $l_f = 1.00$ m; $\circ$ level ice with $d_f = 0.058$ m and $l_f = 2.00$ m; $\diamond$ grease ice with $d_f = 0.021$ m and $l_f = 2.65$ m; and $\square$ nilas ice with $d_f = 0.006$ m and $l_f = 2.69$ m. The solid straight line in (b) is a linear fit (with $R^2 = 0.982$) to the data points. Error bars are omitted from the data points as they were comparable with the marker size.

Figure 2b shows a time series constructed by measuring the temporal changes in image pixel values in a prescribed column at a fixed horizontal coordinate in each frame of the experimental movie over a time interval of 25 s. Such series were used to measure wave amplitude by tracing the vertical disturbance of a streamline at the top ($z = h_3 + h_2$) of the pycnocline from its undisturbed depth to maximal displacement. The time at which the pycnocline reached maximum displacement was also recorded. This process was repeated at three fixed locations $x_{1,2,3}$ over known horizontal distances $\delta x \approx 0.26$ m. The wave phase speed $\delta x/\delta t$ was obtained by noting the time δt between maximal interface displacement at the three fixed locations $x_{1,2,3}$. This process was repeated over all three cameras for waves in which there was no change of form. Average amplitude a and average wave phase speed c were then computed. The half wavelength, λ, was calculated from the time series by measuring the time taken for the pycnocline to be displaced from $z = h_3 + h_2 - a/2$ to $z = h_3 + h_2 - a$, to get a quarter wavelength and then multiplying the result by $2c$.

Figure 2c shows a time series constructed by measuring the temporal changes in image pixel values in a prescribed row of lateral extent $x \in [2.55, 3.06]$ m at a fixed vertical coordinate in each frame of the experimental movie, over a time interval of 25 s. The horizontal slices (which coincide with the ice) are rotated through 90° anticlockwise and ordered sequentially from left to right. In this way the edge of the ice (marked by the interface between black and orange) can be traced. It can be seen that after an initial acceleration (due to the wave motion, cf. Figure 2b), the ice moves at a constant speed before it encounters the end of the wave flume and is arrested. The constant floe speed, c_f, was measured from the gradient of the straight section of the trace indicated by an arrow in Figure 2c.

Figure 3a summarizes the range of wave phase speeds, wave amplitudes, ice types, and dimensions investigated (see supporting information S1 for further details). In Figure 3b the nondimensional floe speed c_f/c versus the nondimensional ice floe length $l_f/2\lambda$ is presented for the level ice cases only. In these cases, the ice floe was relatively long, $l_f/d_f \in [17.2, 73.1]$, and completely free to move. In the grease ice case, the ice was not packed in tight, and there were regions where it was possible to compress the ice but the ice initially extended to the end wall of the flume and hence was only partially free to move in the horizontal direction. Nevertheless, the wave-induced flow transported the grease ice horizontally (at a speed of $c_f/c \approx 0.25$). In the case of the nilas ice, the ice was fixed in the positive horizontal direction (by the end wall of the flume), and hence, there was no wave-induced floe movement. Figure 3b suggests that when the ice is free to move and the floe is relatively long, there is a linear relationship between the wave-induced floe speed and the floe length given by the equation of the plotted straight line, namely, $c_f/c = -0.61 l_f/2\lambda + 0.79$. The wave-induced floe speed was not found to have any dependence on the thickness of the ice floe d_f for the parameter range investigated ($d_f \in [0.013, 0.058]$ m).

3.2. Wave/Ice Edge Interaction

In Figure 4, still images from two experiments in which the ice protruded into the pycnocline are presented. The subpanels are constructed from two overlapping camera outputs. In the smaller wave amplitude case (Figure 4a), the interaction of the wave with the ice edge caused deformation of the wave shape (Figure 4a, (ii)–(iv)), and the wave amplitude was significantly reduced (Figure 4a, (v)), so much so that in this case

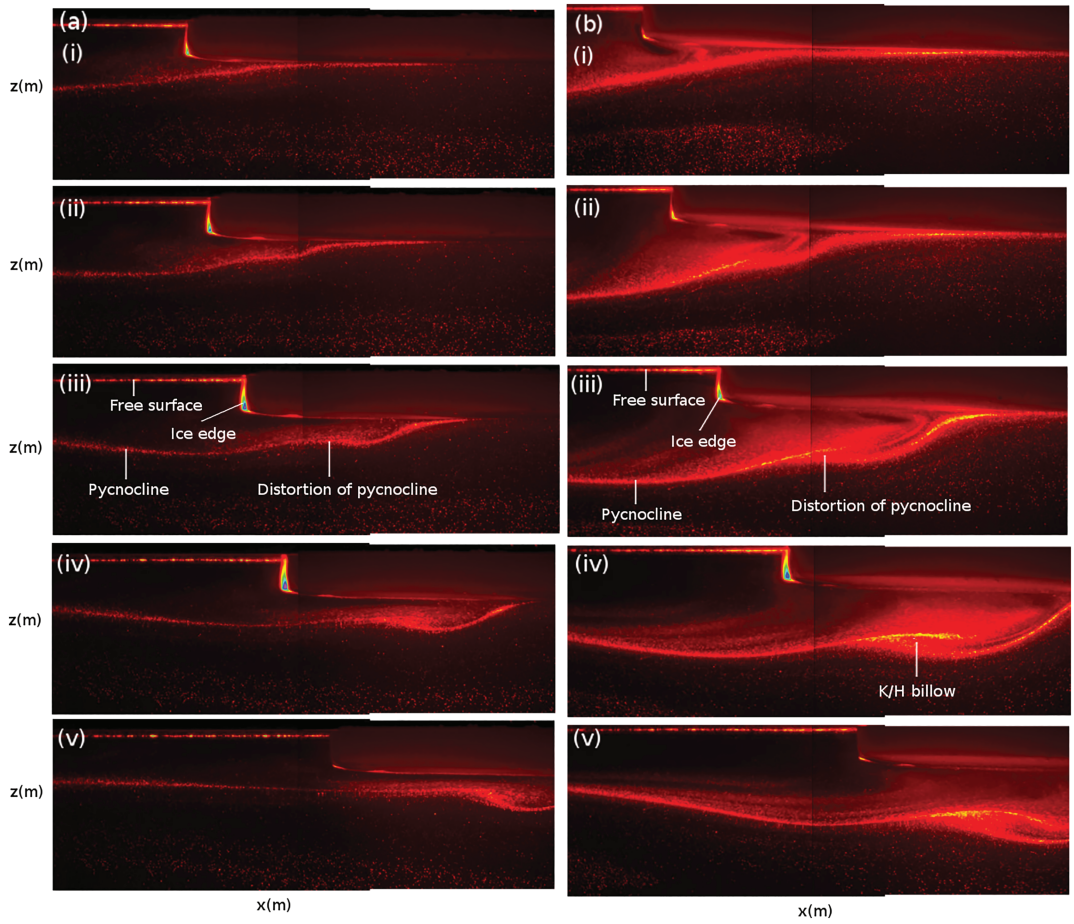

Figure 4. Series of experimental images for an experiment in which the ice was level ice of dimensions $d_f = 0.058$ m and $l_f = 1.00$ m, and the incident ISW had (a) $a = 0.053$ m and (b) $a = 0.113$ m. The images show light intensity and ordered sequentially in time from top to bottom at intervals of $\Delta t = 2.14$ s; subpanel dimensions are $(\Delta x, \Delta z) \approx (0.813$ and 0.74 m). The ISW propagates from left to right.

there was no reflected wave signal off the end wall of the flume. The wave was effectively destroyed by its interaction with the ice edge.

In the larger wave amplitude case (Figure 4b), interaction of the wave with the ice edge caused similar deformation of the wave shape, to the smaller amplitude case, but this time a billow resembling the overturning features associated with a Kelvin-Helmholtz instability (Fructus et al., 2009) occurred on the pycnocline (see Figure 4b, (iv) and (v)). Note that the dynamics in the two cases were similar but the proximity of the ice to the pycnocline in case (a) impeded clear billow formation.

3.3. Dissipation of TKE Under the Ice

The three different ice types had different topographic features and associated roughness on their undersides. For example, the grease ice was lumpy in structure and the nilas ice grew columnar ice crystals down into the water, whereas the underside of the level ice was flat and relatively smooth. In Figure 5, fields of horizontal velocity, u; vorticity, ω; dissipation of TKE, ϵ; and profiles of horizontally averaged TKE dissipation, $\bar{\epsilon}$, are presented for experiments with comparable wave amplitudes and wave shape but under varying ice types. The velocity and vorticity fields were computed via PIV. TKE dissipation was computed from the PIV velocity fields following the direct gradient method given in Doron et al. (2001), using 64×64 point, 75% overlapping, estimation windows. This estimate of dissipation requires the assumption that cross-plane velocity gradients have the same average magnitude as the measured in-plane velocity gradients. This estimate also assumes that the spatial resolution of the measured velocity fields is smaller than, or comparable to, the Kolmogorv scale, which was true in all cases presented here. The mean TKE dissipation, $\bar{\epsilon}$, was

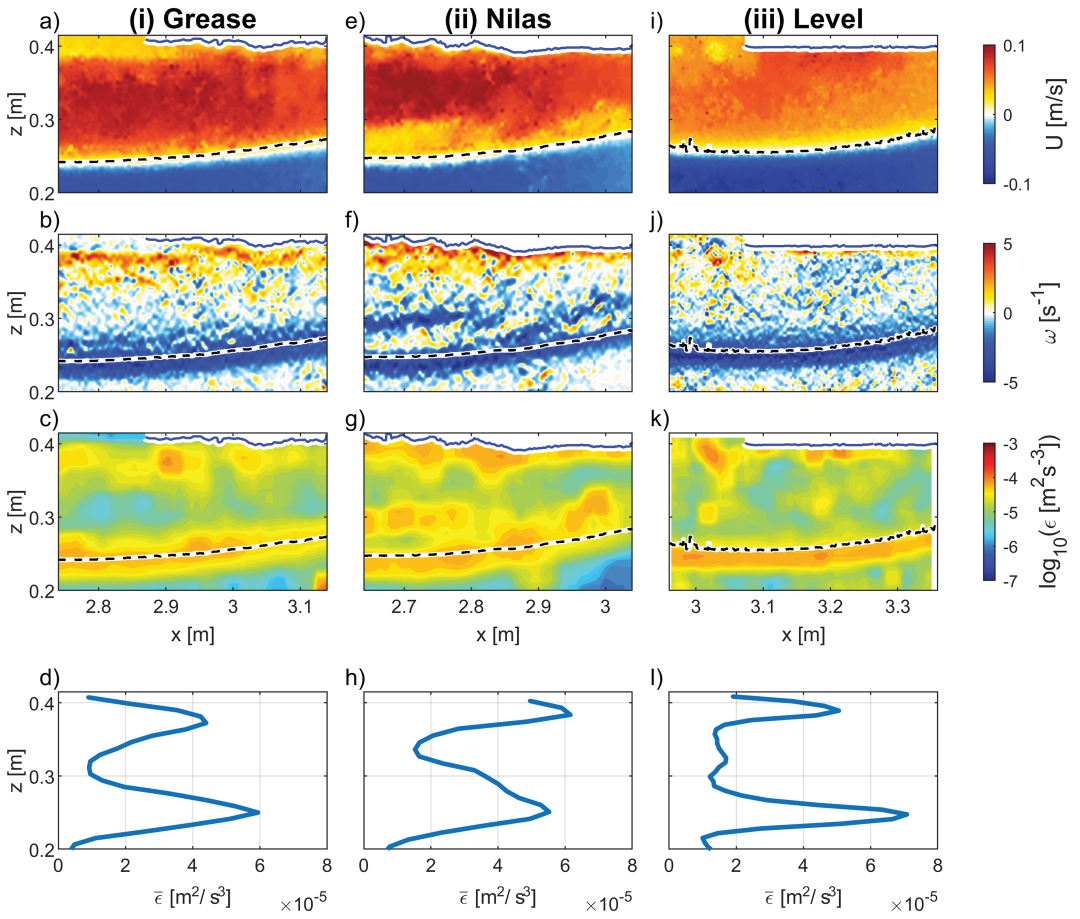

Figure 5. PIV measurements of (a, e, i) horizontal velocity u (m/s), (b, f, j) vorticity ω (s^{-1}), and corresponding calculations of (c, g, k) TKE dissipation $\log_{10}(\epsilon\ (m^2/s^3))$, and (d, h, l) mean TKE dissipation $\bar{\epsilon}\ (m^2/s^3)$ under (i) grease ice (a–d), (ii) nilas ice (e–h), and (iii) level ice (i–l). The black dashed line and the solid blue line depict the top of the pycnocline and the underside of the ice, respectively.

calculated by horizontally averaging the dissipation at every depth bin over the region plotted (minus a small section of width 0.1 m at each side).

The approximate locations of the underside of the ice and the top of the pycnocline were attained by analyzing regions of light intensity in the experimental images. The horizontal velocity plots confirm the findings in section 3.1, that is, the grease ice and level ice were transported horizontally by the wave-induced flow. Enhanced vorticity is seen under the nilas ice when compared with the other cases. This is presumably because the nilas ice was stationary, and hence, the velocity gradient close to the ice, du/dz, is biggest in this case. Moreover, the vorticity plots show that the vertical extent of the vorticity layer directly under the ice is larger in the nilas and grease cases than the level case. This can be attributed to the larger roughness of the grease ice and nilas ice compared to the level ice. Indeed, in these cases, small vortices were seen to form at the underside of the ice downstream of any rough features. The TKE dissipation plots show (in all three cases) that dissipation levels under the ice are comparable with dissipation levels at the pycnocline, suggesting a mechanism for increased IW dissipation and consequently reduced propagation in the ice-covered Arctic Ocean. The mean TKE dissipation profiles confirm that there is a peak in the TKE dissipation below the ice and at the pycnocline. Integration of the TKE dissipation over these two regions of enhanced TKE dissipation give the near-ice dissipation as 77%, 64%, and 54% of the pycnocline value in the grease, nilas, and level ice cases, respectively. Or in other words, dissipation near the ice accounts for approximately 44%, 39%, and 35% of the total dissipation due to turbulence in the grease, nilas, and level ice cases, respectively. The elevated TKE dissipation under the nilas and grease ice hypothesize that a rougher ice bottom and increased vertical shear of horizontal velocity lead to a higher TKE dissipation in the upper boundary layer. Note

that the TKE dissipation measures presented here are true for the experimental conditions tested; whether similar characteristics are seen in the field remains an open question.

4. Relevance to the Field

The interaction of ISWs with an ice edge are expected to be an effective mechanism of dissipating ISW energy and causing localized turbulence and mixing in the field. Similar dissipation is expected beneath any structures (e.g., ice ridge keels or rafted ice) that protrude into the pycnocline. In the field, vortex formation at the underside of the ice surface is expected to contribute further to dissipation of kinetic energy in a similar way to that found at the bottom boundary of the ocean.

The parameter space considered was limited by physical constraints. It differed from the ocean in both Reynolds number, $Re = ac/\nu$ (where ν is kinematic viscosity), and buoyancy frequency

$$N = \sqrt{\frac{-g}{\rho_0}\frac{\partial \rho}{\partial z}}, \tag{1}$$

where g is acceleration due to gravity and ρ_0 is some reference density. Re and N in the laboratory were of the order 10^3 and 1 s^{-1}, respectively. In the Arctic Ocean, when stratification is at its strongest, corresponding values are of the order 10^6 and 0.01 s^{-1}, respectively. Hence, to understand whether the laboratory results scale to the ocean requires variation of Re and N in the future. Moreover, study over a wider range of d_f/h_1 and $l_f/2\lambda$ would provide better insight into field scale dynamics.

The wave phase speed, c, in the experiments was $O(0.1)$ m/s and is comparable to field values which are typically 0.2–0.5 m/s in the Arctic Ocean. The experiments were conducted in a flume at rest; hence an inference regarding Froude number, Fr (ratio of inertia to the external gravity field), is not relevant. The experiments can, however, be compared to nonlinear lee waves in the field (Rippeth et al., 2017) once the initially trapped and steepened wave (which has a $Fr \approx 1$) is released and allowed to propagate in subcritical conditions ($Fr < 1$).

5. Conclusion

The ISW-induced current was shown to transport ice horizontally, and the transport speed of relatively long ice floes was linearly dependent on the floe length for the parameter range considered. When the ice protruded into the pycnocline, interaction of the wave with the ice edge resulted in a Kelvin-Helmholtz billow forming on the pycnocline and the resulting wave signal being deformed or destroyed. If the underside of the ice was rough, boundary layer development due to the ISW-induced flow was observed, and finally, it was shown that levels of TKE dissipation under the ice were comparable to those at the pycnocline. The parameter range investigated was limited by the scale of the facility, but nevertheless the observations show that the physical interactions of ISWs with ice could have important implications for dissipation of wave energy and consequent mixing in the polar oceans and point to the need for further more detailed investigations. Moreover, the observation that an ISW can transport ice horizontally suggests that a series of ISWs may well constitute a mechanism by which sea ice banding can occur as proposed theoretically by Saiki and Mitsudera (2016).

Acknowledgments
The work described in this publication was supported by the European Community's Horizon 2020 Research and Innovation Programme through the grant to HYDRALAB-PLUS, Contract 654110. This work received funding from the MASTS pooling initiative (The Marine Alliance for Science and Technology for Scotland), and their support is gratefully acknowledged. MASTS is funded by the Scottish Funding Council and contributing institutions. The authors thank Nis Schnoor and Gesa Zimmer for providing technical assistance at HSVA, Hamburg, and Prof. Tom Rippeth (University of Bangor) for useful discussion of the work. The EPSRC UK Fluids Network is also thanked for providing funds to disseminate the findings of this work. The data that supports this work can be accessed at the following DOI: 10.5281/zenodo.2574580. The authors thank two anonymous referees whose comments have led to improvements in the paper.

References

Czipott, P. V., Levine, M. D., Paulson, C. A., Menemenlis, D., Farmer, D. M., & Williams, R. G. (1991). Ice flexure forced by internal wave packets in the Arctic Ocean. *Science*, *254*, 832–835.

D'Asaro, E. A., & Morison, J. H. (1992). Internal waves and mixing in the Arctic Ocean. *Deep Sea Resarch Part II*, *39*, S459–S484.

Dalziel, S. B., Carr, M., Sveen, J. K., & Davies, P. A. (2007). Simultaneous synthetic schlieren and PIV measurements for internal solitary waves. *Measurement Science and Technology*, *18*, 533–547.

Doron, P., Bertuccioli, L., Katz, J., & Osborn, T. R. (2001). Turbulence characteristics and dissipation estimates in the coastal ocean bottom boundary layer from PIV. *Journal of Physical Oceanography*, *31*, 2108–2134.

Evers, K.-U. (2015). Modeling ice processes in laboratories and determination of model ice properties. In P. Langhorne (Ed.), *Cold regions science and marine technology*, Encyclopedia of Life Support Systems (EOLSS). Paris, France: EOLSS Publishers.

Fer, I. (2009). Weak vertical diffusion allows maintenance of cold halocline in the central Arctic. *Atmospheric and Oceanic Science Letters*, *2*, 148–152.

Fer, I. (2014). Near-inertial mixing in the central Arctic Ocean. *Journal of Physical Oceanography*, *44*, 2031–2049.

Fer, I., Skogseth, R., & Geyer, F. (2010). Internal waves and mixing in the marginal ice zone near the Yermak Plateau. *Journal of Physical Oceanography*, *40*, 1613–1630.

Fructus, D., Carr, M., Grue, J., Jensen, A., & Davies, P. A. (2009). Shear induced breaking of large amplitude internal solitary waves. *Journal of Fluid Mechanics*, *620*, 1–29.

Guthrie, J., Morison, J. H., & Fer, I. (2013). Revisiting internal waves and mixing in the Arctic Ocean. *Journal of Geophysical Research: Oceans*, *118*, 3966–3977. https://doi.org/10.1002/jgrc.20294

Kirillov, S. (2006). Spatial variations in sea-ice formation-onset in the Laptev Sea as a consequence of the vertical heat fluxes caused by internal waves overturning. *Polarforschung*, *79*, 119–123.

Kozlov, I. E., Kudryavstev, V. N., Zubkova, E. V., Atadzhanova, O., Zimin, A. V., Romanenkov, D., et al. (2015). SAR observations of internal waves in the Russian Arctic Seas. In *2015 IEEE International Geoscience and Remote Sensing Symposium (IGARSS)*, Milan, Italy, pp. 947–949.

Kozlov, I. E., Romanenkov, D., Zimin, A. V., & Chapron, B. (2014). SAR observing large-scale nonlinear internal waves in the White Sea. *Remote Sensing of Environment*, *147*, 99–107.

Kozlov, I. E., Zubkova, E. V., & Kudryavstev, V. N. (2017). Internal solitary waves in the Laptev Sea: First results of spaceborne SAR observations. *IEEE Geoscience & Remote Sensing Letters*, *14*, 2047–2051.

Levine, M. D., Paulson, C. A., & Morison, J. H. (1985). Internal waves in the Arctic Ocean: Comparison with lower-latitude observations. *Journal of Physical Oceanography*, *15*, 800–809.

Lincoln, B. J., Rippeth, T. P., Lenn, Y.-D., Timmermans, M. L., Williams, W. J., & Bacon, S. (2016). Wind-driven mixing at intermediate depths in an ice free Arctic Ocean. *Geophysical Research Letters*, *43*, 9749–9756. https://doi.org/10.1002/2016GL070454

Marchenko, A. V., Morozov, E. G., Muzylev, S. V., & Shestov, A. S. (2010). Interaction of short internal waves with ice cover in an Arctic fjord. *Oceanology*, *50*, 18–27.

Muench, R. D., LeBlond, P. H., & Hachmesiter, L. E. (1983). On some possible interactions between internal waves and sea ice in the marginal ice zone. *Journal of Geophysical Research*, *88*, 2819–2816.

Munro, R. J., & Davies, P. A. (2009). The flow generated in a continuously stratified rotating fluid by the differential rotation of a plane horizontal disc. *Fluid Dynamics Research*, *38*(8), 522–538.

Padman, L., & Dillon, T. M. (1991). Turbulent mixing near Yermak Plateau during the coordinated eastern Arctic experiment. *Journal of Geophysical Research*, *96*, 4769–4782.

Rainville, L., & Winsor, P. (2008). Mixing across the Arctic Ocean: Microstructure observations during the Beringia 2005 expedition. *Geophysical Research Letters*, *35*, L08606. https://doi.org/10.1029/2008GL033532

Rippeth, T. P., Lincoln, B. J., Green, J. A. M, Sundfjord, A., & Bacon, S. (2015). Tide-mediated warming of Arctic halocline by Atlantic heat fluxes over rough topography. *Nature Geoscience*, *8*, 191–194.

Rippeth, T. P., Vlasenko, V., Stashchuk, N., Scannell, B. D., Green, J. A. M., Lincoln, B. J., & Bacon, S. (2017). Tidal conversion and mixing poleward of the critical latitude (an Arctic case study). *Geophysical Research Letters*, *44*, 12,349–12,357. https://doi.org/10.1002/2017GL075310

Saiki, R., & Mitsudera, H. (2016). A mechanism of ice-band pattern formation caused by the resonant interaction between sea ice and internal waves: A theory. *Journal of Physical Oceanography*, *46*, 583–600.

Sandven, S., & Johannessen, O. M. (1987). High-frequency internal wave observations in the marginal ice zone. *Journal of Geophysical Research*, *92*, 6911.

Vlasenko, V., Stashchuk, N., Hutter, K., & Sabinin, K. D. (2003). Nonlinear internal waves forced by tides near the critical latitude. *Deep Sea Research Part I*, *50*, 317–338.

Zimin, A. V., Kozlov, I. E., Atadzhanova, O. A., & Chapron, B. (2016). Monitoring short-period internal waves in the White Sea. *Izvestiya, Atmospheric and Ocean Physics*, *52*, 951–960.